The Thesis Committee for Thomas Frederick Pizarek certifies that this is the approved version of the following thesis:

Improved Lumped-Parameter Model for Acoustic Monitoring of Tension in a Timing Belt Used in Automated Material Handling Systems

APPROVED BY

SUPERVISING COMMITTEE:

Preston S. Wilson, Supervisor

Dragan Djurdjanovic, Supervisor

Improved Lumped-Parameter Model for Acoustic Monitoring of Tension in a Timing Belt Used in Automated Material Handling Systems

by

Thomas Frederick Pizarek, B.A.

THESIS

Presented to the Faculty of the Graduate School of

The University of Texas at Austin

in Partial Fulfillment

of the Requirements

for the Degree of

MASTER OF SCIENCE IN ENGINEERING

THE UNIVERSITY OF TEXAS AT AUSTIN

August 2011

Improved Lumped-Parameter Model for Acoustic Monitoring of Tension in a Timing Belt Used in Automated Material Handling Systems

Thomas Frederick Pizarek, M.S.E.
The University of Texas at Austin, 2011

Supervisors: Preston S. Wilson
Dragan Djurdjanovic

Automated Material Handling Systems are practically ubiquitous across industry and many rely on the operation of timing belt drives, which require that the belt be tensioned properly in order to function correctly. A series of experiments was carried out in which the frequency spectrum of acoustic radiation caused by transverse vibrations of a timing belt was used to calculate the belt tension. A lumped-parameter model was developed that considers the geometric complexity of the timing belt's construction by calculating the stiffness of a single belt tooth using commercially-available finite element analysis software. This was used to modify the belt's effective stiffness suggested by the manufacturer. Based on the experimental data, a set of material parameters was determined that, when used in the lumped-parameter model, resulted in tension predictions that agreed with the experiment within the 95% confidence intervals of the means.

Table of Contents

Abstract **iv**

List of Figures **vii**

Chapter 1. Introduction **1**
1.1 Automated Material Handling Systems 1
1.2 Timing Belt Drives 2
1.3 Organization of Thesis 4

Chapter 2. Belt Models **5**
2.1 Literature Review 5
2.2 Models Used in This Work 13
2.2.1 Effective Spring Model 14
2.2.2 Tooth Stiffness 15

Chapter 3. Experimental Apparatus **21**
3.1 Variables to be Controlled 21
3.2 Description of Experimental Apparatus 23

Chapter 4. Experimentation **26**
4.1 Simple String Experiment 26
4.1.1 Additional Apparatus 27
4.1.2 Procedure 28
4.2 Belt Experiment 29
4.2.1 Additional Apparatus 29
4.2.2 Procedure 29
4.3 Data Processing 30
4.3.1 Examples of Raw Data 30
4.3.2 Processing Algorithm 35

4.4 Results 40
4.4.1 String 40
4.4.2 Belt 41

Chapter 5. Comparison of Measurements to Models **44**
5.1 String Experiment 44
5.2 Belt Experiment 46

Chapter 6. Conclusions and Future Work **51**
6.1 Conclusions 51
6.2 Future Work 52

Bibliography **54**

Vita **59**

List of Figures

1.1 An illustration of the construction of the timing belt used in this thesis. 2

2.1 A diagram of the belt's tooth profile. 14
2.2 An illustration of the multi-spring model. 15
2.3 The geometry of the belt tooth used in finite element modeling. 17
2.4 The results of the finite element analysis of a single tooth subjected to edge loads. 20

3.1 A string with fixed boundaries of length L, struck at x_0 with velocity u_0. 22
3.2 A schematic diagram of the experimental apparatus. 24

4.1 An example of the time series data collected in the simple string experiments. 31
4.2 A spectrogram of the time series data shown in Figure 4.1 (simple string). 31
4.3 An example of the time series data collected in the belt vibration experiment with the IVD centered on the belt face. 33
4.4 An example of the time series data collected in the belt vibration experiment with the IVD positioned at 5/17 of the width of the belt face. 33
4.5 A spectrogram of the time series data shown in Figure 4.3 (timing belt excited on center). 34
4.6 A spectrogram of the time series data shown in Figure 4.4 (timing belt excited off-center). 34
4.7 The Fast Fourier Transform (FFT) of the data shown in Figure 4.1 (simple string). 36
4.8 The FFTs of the timing belt data shown in Figure 4.3 (on-center excitation) and Figure 4.4 (off-center excitation). 37
4.9 Measured tensions from the simple string experiments. 40

4.10 Measured from the belt vibration experiment with the IVD centered on the belt face. 42
4.11 The mean values of the measured tensions from the belt vibration experiments with the IVD positioned at 5/17 of the width of the belt face. 43

5.1 The results of the simple string experiment with predictions based on an effective spring model. 45
5.2 Comparison of the means of the measured tensions from all belt experiments, both on- and off-center to the predictions based on the finite element method simulation. 47
5.3 The results of the belt vibration experiment with the IVD centered compared to predictions based on the manufacturer's single spring model and the three spring model with tooth stiffness included. 49
5.4 The results of the both belt vibration experiments compared to predictions based on the model with tooth stiffness included. . 50

Chapter 1

Introduction

1.1 Automated Material Handling Systems

Automated Material Handling Systems (AMHS) are widely used in a variety of industries, including: health care, distribution (notably including postal services [1]), apparel, automotive, and all manner of manufacturing [2]. The growing dependence of industry on AMHS is suggested by the fact that the revenue of the top 20 AMHS suppliers increased from $9.8 billion in 1999 [3] to $15.3 billion in 2008 [4]. AMHS are employed by the semiconductor manufacturing industry in order to increase yield and reduce cycle times while simultaneously addressing concerns about ergonomics and contamination [5].

This thesis is concerned with the belt that drives a tool called a stocker in a semiconductor manufacturing AMHS. The function of a stocker in a semiconductor manufacturing line is to act as a buffer between intra-bay and inter-bay transport systems. As a wafer undergoes hundreds of processes involving about 250 tools [5], the stocker ensures that the wafers are delivered to the proper tools at the proper times to minimize tool downtime. When a stocker fails, the flow of material is interrupted, resulting in blockages and costly downtime. The reliability of this integral part of the AMHS requires proper

maintenance of the timing belt that drives the robot responsible for the storage and retrieval of material.

1.2 Timing Belt Drives

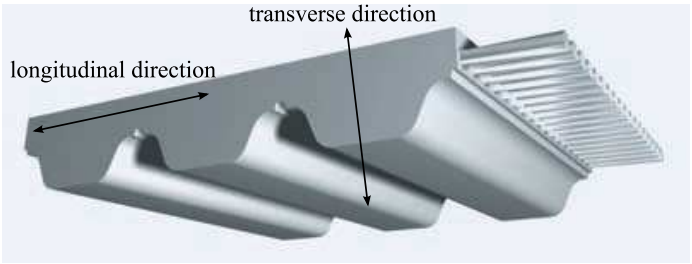

Figure 1.1: An illustration of the construction of the timing belt used in this thesis. A portion of the belt is cut away to show how the tension members are embedded in the molded polyurethane matrix. The directions of transverse and longitudinal vibrations are indicated with arrows. [6]

The belt used in this thesis consists of a large number of braided steel tension members laid in parallel across the width of the belt embedded in a thermoplastic polyurethane matrix with molded teeth, as shown in Figure 1.1. The composite construction of this belt complicates the modeling of its behavior. The belt profile, non-uniform spacing of tension members across the belt width, nonlinear material properties of polyurethane, and interface between the steel and the polyurethane matrix make modeling from first principles difficult.

Timing belt drives employ toothed pulleys and belts to transfer power in a manner similar to that of chain drives. The transmission of power relies on the interaction between the teeth on the pulleys and the teeth on the belt.

Timing belt drives are preferred to flat belt and V-belt drives in applications where positional accuracy is important because they eliminate the cumulative errors due to slip [7]. This aspect is especially important in the application considered here, because the stocker must be able to retrieve materials from storage areas and deliver them to precise locations. The ability of the belt to perform depends on the tension that it is under. If the tension is too high, then the pulley shaft bearings will be overloaded, causing increased wear; if the tension is too low, then tooth jumping may occur, which causes (at the least) a loss of positional accuracy [8].

A timing belt may fail in a variety of ways. If the tension is too high, there may be excessive wear in the land areas of the belt, and tooth roots may crack. If the tension is too low, then the belt teeth will not sit properly in the pulley, rising up out of the grooves. Then the drive load will not be applied to the root of the tooth, causing the tooth to bend. This may cause strips of teeth to separate from the belt. Additionally, low tension may lead to tooth jump, which can lead to damage of the belt's tension members in addition to the loss of positional accuracy. Another source of belt failure is pulley misalignment. When pulleys are angularly misaligned, then one side of the belt will carry a higher tension than the other, often resulting in tooth root cracks on the side with the higher tension. [9]

Clearly, the tension in the belt is of prime concern from performance and maintenance perspecitves. The models and experiments presented in this thesis represent a part of a research initiative to improve the current belt

tension monitoring methodology. Typically, tension is monitored acoustically. Transverse vibrations are excited by manually plucking the timing belt, and a microphone records the radiated acoustic pressure. For example, if the timing belt behaved as a simple string, the frequency of the response would be related to the tension by the equation $T = \rho_\ell (2Lf_n/n)^2$, where T is the string tension, ρ_ℓ is the linear mass density of the string, L the length of the vibrating span, and f_n is the frequency of the n^{th} mode of vibration. As described at length in [10], acoustic tension monitoring as currently used in industry requires improvement, with typical systems reporting both false positives and false negatives at an unacceptable rate. This thesis is focused on investigating an improved mathematical model to relate the longitudinal deflection of a belt to its tension in a manner consistent with an acoustic tension test.

1.3 Organization of Thesis

The rest of the thesis is organized as follows. Chapter 2 reviews the current state of the art in belt tension monitoring and belt drive modeling and also presents the models that will be used in this paper. Next, Chapter 3 describes the apparatus used in the experiments. Chapter 4 reports on the experiments performed. Simple string experiments are presented in order to validate that the experimental apparatus controls force as anticipated, in a linear manner. In Chapter 5, the results of the experiments are compared to model predictions. Chapter 6 presents concluding remarks and suggestions for future work.

Chapter 2

Belt Models

2.1 Literature Review

As outlined in Chapter 1, timing belts are versatile and their use is important in many industries. However, their successful operation depends on proper installation and maintenance, with the most crucial factor being the belt tension. Thus, there is a need to be able to monitor the tension reliably and to model the tension accurately. Successfully modeling the tension in a belt span is an integral part of the modeling of belt drive mechanics. This section will provide an overview of the progression of tension monitoring techniques and belt drive modeling.

The simplest method for monitoring tension is the 3-point bending test. A transverse load is applied to the belt and its transverse deflection is measured (see Figure 1.1 and Figure 2.1 for clarification of the transverse direction). Then, empirical formulae or tabulated values are used to relate these quantities to the belt tension. A typical formula can give estimates that are up to 60% lower than the actual tension [8]. This method is sensitive to deflection location and devices that perform this test can significantly alter the tension in the belt during measurement [8]. This method was revisited by

Melas *et al.* [11] in 2004. The authors applied a transverse load to the midpoint of a belt span and used a linear variable displacement transducer (LVDT) and a spring balance to calculate the transverse displacement as a function of the force applied. From this, they calculated the axial tension in the belt and, subsequently, the belt span's natural frequency. The results of these tests were compared to frequency spectra of the belt span when manually vibrated, as measured by accelerometer and by a proximity transducer. The accelerometer and proximity transducer gave consistent results, but the deflection method underestimated the natural frequency of the belt span by over 13%. While this method did not give an accurate measurement, the authors maintained that it would be effective in determining changes in belt tension that would portend failure.

As implied in the discussion of the work of Melas *et al.*, it is possible to estimate the tension in the belt from the fundamental frequency of its free transverse vibrations (and vice versa) using the one-dimensional wave equation. This was first demonstrated by Fawcett *et al.* [8], whose experimental results showed that, for a toothed belt, there is a linear relationship between tension and the square of the fundamental frequency of transverse vibration. The results improved for longer belt spans over the examined range of 150 mm to 350 mm. In this model, the belt is assumed to be homogeneous, isotropic, linearly elastic, and free of damping. These assumptions are counterindicated by the construction of a composite belt. The fact that there are stiff tension members laid parallel in a soft matrix guarantees heterogeneity and anisotropy.

Additionally, the use of a polymer such as rubber or polyurethane as the matrix introduces nonlinear elastic behavior and frequency-dependent damping [12]. Despite these drawbacks, this method remains the most common.

The above is essentially the extent of the literature that is concerned with stationary belt spans alone; the remainder of the section is concerned with models of belt drive systems. There are four primary subjects of study in the modeling of belt drives. First, while a belt drive is in motion, there must be a tension differential between the belt spans on opposite sides of a pulley. This phenomenon can be explained by creep theory or shear theory. Using either creep theory or shear theory, the physical mechanism that causes the tension differential is friction, the second topic of interest, which is modeled using Coulomb friction or a creep-rate-dependent (i.e., sliding-velocity-dependent) law. The third concern of belt drive modeling is the significance of the physical parameters of the belt—for example the axial stiffness, flexural stiffness, shear stiffness, mass, and damping characteristics. The fourth primary interest is in the mechanisms that excite transverse vibrations in the belt.

The distribution of the belt tension and tooth load in a two-pulley timing belt drive system in a quasi-static state was addressed by Gerbert *et al.* [13]. They modeled the belt links and teeth as springs and calculated the distribution of the load across the portion of the belt that engages the toothed pulley. The authors used a finite element model of one pitch of a belt, including the tooth and the cord, to determine the spring constant of the tooth. The results of the finite element model were found to be in good

agreement with experimental results. However, the predictions of the tension distribution were greater than the values measured by strain gauges, though they followed the same general trend. The authors suggested that the reason for the discrepancies may have been irregularities in the pitch of the belt and the pulleys.

Next, researchers have modeled the dynamics of a belt drive in a steady state. That is, a continuously circulating belt in a system of pulleys. For steady state models, the driven pulley is assumed to have a constant angular velocity, or appply a steady torque. In 1970, Firbank [14], introduced shear theory as an alternative to the long-standing creep theory originated by Osborne Reynolds [15]. Creep theory assumes that the belt is flexible, extensible, and thin enough that bending and shear strains are negligible. Then, when there is a change in belt tension due to friction, the belt extends or contracts elastically and moves relative to the surface of the pulley. Firbank argued that the assumptions of this theory no longer hold due to advances in belt construction. The tension members of modern belts are essentially inextensible in the longitudinal direction—especially when compared to the cotton and leather belts in use when creep theory was developed. Therefore, Firbank suggested that friction between the pulley and the belt causes shear deformation in the matrix surrounding the tension members. This shearing of the extensible matrix causes a tension change in the embedded load-carrying members.

Alciatore *et al.* [16] have extended the analytical models of creep theory and shear theory for use in systems with an arbitrary number of pulleys, using

a Coulomb friction paradigm. Additionally, the authors discussed the effects of bending stiffness and centrifugal forces. Specifically, for a thick belt rounding a pulley, the increase in tension due to bending stiffness is approximately linearly related to the reciprocal of the diameter of the pulley. Centrifugal forces were considered for cases when the belt mass is significant or belt speeds are high. These forces cause an increase in the belt tension and a decrease in the pressure at the belt-pulley interface. This implies that the belt's inertia causes it to tend to travel tangent to the pulley, but tension will pull it back toward the tangent line between two pulleys, which results in transverse motion. This work laid the foundation for identifying mechanisms that cause transverse belt vibrations.

Li and Chen [17], extending the work of Beikmann *et al.* [18] and Parker [19], derived the explicit characteristic equation of a serpentine belt drive system with two pulleys and a tensioner arm. Modeling of a serpentine belt drive is generally not concerned with the belt-pulley interaction; thus, this work does not address creep theory, shear theory, or friction concerns. The belt is treated as a string, neglecting bending stiffness, shear deformation, and damping.

Zhang and Zu [20] considered the free vibrations of a moving viscoelastic belt. The treatment is not defined in terms of belt drives, so the belt-pulley interface was not considered. Coriolis and centripetal acceleration components were included and the Kelvin viscoelastic model was used, but flexural and shear effects were neglected. The Kelvin model describes the viscoelastic

property of a material as a linear spring and a linear damper connected in parallel. The results of Zhang and Zu's analysis showed that the damping introduced by the viscoelastic model has no significant effect (to a first order approximation) on the natural frequencies of the free vibration, although it does cause the amplitude of the response to decrease more quickly with time. Conversely, varying the elastic stiffness parameter does move the natural frequencies, but does not affect the free response amplitude. According to linear theory, the location and amplitude of resonant peaks are coupled. The analysis also found that the natural frequencies decrease as the belt's translation speed is increased, which is consistent with linear theory.

An analytical model for a flat belt was developed by Leamy and Wasfy [21], using a creep-rate-dependent, trilinear friction law instead of Coulomb friction. This model was chosen for its physical relevance, especially for small sliding velocities, and its computational convenience—it eliminates the discontinuity present in classical Coulomb friction theory. Closed-form expressions were found for the tension distribution and sliding-zone arc magnitudes for a two-pulley belt drive. Under a Coulomb friction law, one expects to observe two distinct zones in the arc of contact between the pulley and the belt: an adhesion zone in which the belt and pulley are moving with the same velocity, and a slip zone in which the belt and pulley are sliding past one another. However, the creep-rate-dependent friction law resulted in no adhesion zones whatsoever. In fact, depending on the slope of the friction law profile, there may be two distinct sliding zones on one or both of the pulleys. The analytical results

were found to agree well with a finite element model.

Recently, groups have derived models of the transient behavior of belt drives. Leamy and Wasfy [22] devised a time-accurate finite element model for the representation of timing belts and serpentine belts (as a special case of the timing belt with no teeth). The belt was modeled using beam elements, including axial and bending stiffnesses. The teeth of the pulley were treated as internal, thus lumping together the compliances of the belt teeth and pulley teeth. A modified version of the creep-rate-dependent friction law introduced in [21] was used to model the belt-pulley interface. The finite element model was validated with the analytical model of [21] for the serpentine belt in the steady state and with available experimental data for the timing belt.

Čepon *et al.* [23] developed a nearly comprehensive finite element model. The belt was modeled as a planar beam element, including axial stiffness, flexural stiffness, and viscoelasticity properties, but no shear deformation. The authors used a discontinuous Coulomb law to model the belt-pulley contact, citing that it is more accurate than the trilinear creep-rate-dependent laws. Coriolis forces were included and pulley eccentricity was introduced by allowing the axis of rotation to be specified away from the pulley's geometric center. These effects introduce transverse oscillations in the belt spans. The authors noted peaks in the normal and tangential forces at the entry and exit sections of the belt and non-zero friction forces at the beginning of the adhesion zones. These phenomena were attributed to bending stiffness in the belt.

A lumped-parameter finite element model of the behavior of timing belt

drives was proposed by Callegari *et al.* [24]. Spring and damper elements were used to describe the stiffnesses and damping behaviors in the axial and bending reactions. The contact forces between the flanks of a belt tooth and a pulley tooth, the tip of a belt tooth and the bottom land of the pulley, and the back side of the belt and an idler or tensioner pulley (with no teeth) were considered. In this model, tooth geometry, rather than friction, accounts for the transfer of power from the pulley to the belt. The inertia of the belt elements was included and the model allowed for the user to specify either the rotational velocity or the torque applied to the driver and driven pulleys. Along with belt inertia and pulley eccentricity, tooth meshing and time-varying pulley loads were validated as sources of transverse vibrations. The model resulted in simulated sound power levels that exhibited the same trends as experiments, but had values about 12 dB higher. The authors ascribed this discrepancy to the linearization of the lumped parameters. The results of this study and of [22] are in good agreement, indicating that tooth geometry supplants friction as the mechanism of power transfer in timing belt applications.

To summarize the findings of the models discussed, one can conclude that transverse vibrations—which cause acoustic radiation—are a natural phenomenon in belt drives. See Figures 1.1 and 2.1 for clarification of the direction of transverse oscillations. The frequency of transverse vibrations is largely dependent on belt tension, geometry, and material. For flat belt and V-belt drives, the mechanism by which power is transferred between the pulley and the belt is friction, which can be described using the classical Coulomb model

or a creep-rate-dependent model. In timing belt applications, however, the role of friction is largely replaced by tooth geometry. Elastic stiffness and damping are found to be more important to the accuracy of belt modeling than flexural or shear effects because timing belts and flat belts tend to be thin, rendering these effects negligible. However, bending and shear stiffnesses become important when dealing with belts with thick profiles, such as V-belts. The Kelvin viscoelastic model has been used to incorporate damping, showing that the damping parameter has no significant effect on the natural frequencies of belt vibration, but does cause the vibration amplitude to decay more quickly with time. Transverse belt vibrations have been found to be caused by belt inertia, pulley eccentricity, non-constant pulley loads, and tooth meshing.

For another treatment of the literature that includes more detail on experimental methods and results, the interested reader is referred to the master's thesis of Musselman [10].

2.2 Models Used in This Work

As mentioned in Section 2.1, there are few models that reflect the way in which belt tension is currently monitored—by measuring the frequency of acoustic radiation of a belt span while the drive is not in operation—and there is also little experimental verification of these models. Additionally, extant models that relate tension to longitudinal deflection are inconsistent with acoustic tension tests. In the work presented here, this deficiency is addressed through the investigation of an existing model and the development

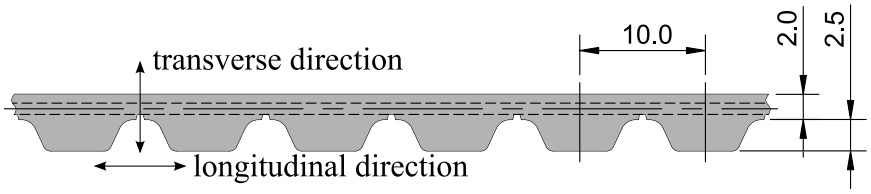

Figure 2.1: A diagram of the belt's tooth profile. Note the arrows representing the directions of transverse and longitudinal vibrations. The dashed lines indicate the region occupied by the steel tension members. The dimensions shown are in mm. [6]

of an improved model.

The timing belt that was used in the experiments for this thesis is 1 m long and 75 mm wide, consisting of 51 steel tension members, varying in diameter between 0.89 and 1.14 mm, embedded in thermoplastic polyurethane. The pitch of the belt—the distance from the center of one tooth to the center of the next—is 10 mm, with profile shown in Figure 2.1. In order to reflect the conditions under which the belt tension is currently monitored, the belt has been treated as stationary.

2.2.1 Effective Spring Model

The manufacturer of the belt suggests that it be modeled as an effective spring, and provides a specific belt stiffness of $k_{\text{spec}} = 4.25 \times 10^5$ N/10 mm of belt width. Multiplying this by the width of the belt (75 mm) and dividing by the effective length of the belt, L, results in an effective spring constant, $k_{\text{belt}} = (3.19 \times 10^6)/L$ N/m [6]. Then, it is straightforward to use Hooke's law to calculate the tension in the belt based on its axial deflection.

This model assumes that the composite construction and geometric complexity of the belt may be ignored, and that it may be treated as an equivalent homogeneous material that behaves linearly, that is, it obeys Hooke's law.

2.2.2 Tooth Stiffness

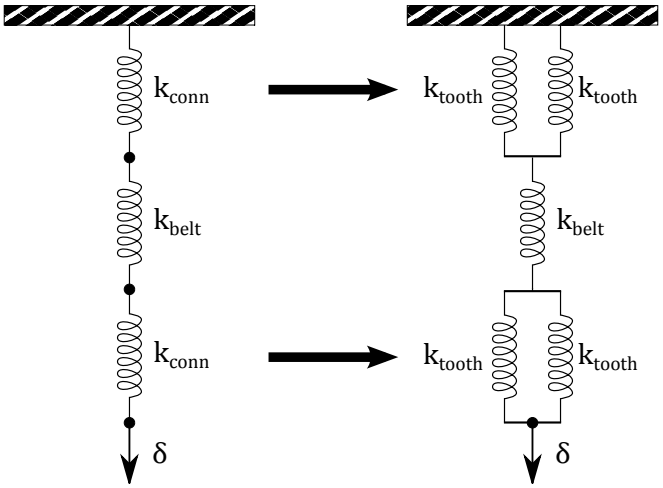

Figure 2.2: An illustration of the model that includes the stiffness of the connection between the belt and the clamps, k_{conn}, in addition to the stiffness of the belt k_{belt}. As shown in the drawing on the right, each of the connection stiffnesses are modeled as two tooth stiffnesses in parallel.

The model proposed here drew inspiration mainly from concepts out of the works of Gerbert *et al.* [13] and Callegari *et al.* [24], with the goal of making a significant improvement to the model discussed in the previous section as simply as possible. The belt remains treated as a string, neglecting all flexural and shear effects. This is justified because the belt is thin, has a long span, and is under high tension, thus any correction to the natural frequencies of the belt is likely to be negligible [25]. Damping is also neglected, which is

reasonable because we are cheifly concerned with the natural frequencies of the belt, which are not significantly affected by damping, as shown by Zhang and Zu [20].

The manufacturer's model was modified by incorporating the effects of the geometric complexity of the belt. The tension in the span of the belt and the load on a tooth are closely related [26], so the stiffness of the connection between the belt and the pulley or clamp must be addressed. In the experiments described in the following sections, a belt sample is clamped at both ends, and put under tension. To account for this configuration, two stiffnesses representing the mechanical connections between the belt and the clamps are added to the effective stiffness suggested by the manufacturer, similar to techniques used in [22] and [24]. The resulting system can be visualized as three springs connected in series, as shown in Figure 2.2. This configuration results in a modified effective spring constant,

$$k_{\text{eff}} = \frac{1}{\frac{1}{k_{\text{belt}}} + \frac{2}{k_{\text{conn}}}} \tag{2.1}$$

where k_{conn} is the stiffness of the belt-clamp connection. This connection stiffness, k_{conn} itself, was modeled as two springs in parallel, representing the stiffnesses of the first two teeth engaged by the clamp, each of which have a stiffness that is determined by the finite element model described in the following paragraphs.

An individual tooth was modeled using commercially-available finite

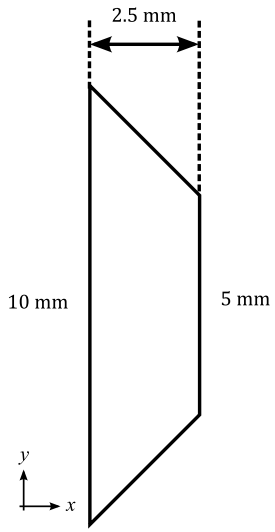

Figure 2.3: The geometry of the belt tooth used in finite element modeling.

element analysis software in order to determine an effective stiffness. The tooth's shape was simplified to a regular trapezoid, ignoring any curvature in the profile—see Figure 2.3. The tooth was constrained such that it was allowed to move in the y-direction only. Distributed loads were applied to the back face of the tooth according to $\vec{P}_{\text{back}} = F_0/(7.5 \times 10^{-4})\hat{y}$, and to the top angled face according to the formula $\vec{P}_{\text{top}} = -F_0/[(2.5\sqrt{2})7.5 \times 10^{-7}]\hat{y}$, where F_0 is the nominal force applied and the denominators of these expressions are equal to the areas of the respective faces, such that the total force on the boundaries was zero. The finite element analysis software requires the density (ρ), Young's modulus (E), and Poisson's ratio (ν) for all solid materials in the simulation. It was assumed that the polyurethane is isotropic and linearly elastic; these assumptions are not true in general, but they are reasonable for the static case considered here. While the software calls for the density of the

material to be specified, it was found that the value used was not important in the static simulations. Values from 300 kg/m^3 to 1000 kg/m^3 (a typical value for polyurethanes [27]) were used in the simulations with no effect on the results.

The manufacturer reports the hardness of the polyurethane as 92 Shore A [6]. From this, it is possible to calculate the Young's modulus of the material based on the relation derived by Gent [28]:

$$E = \frac{0.0981(56 + 7.66S)}{0.137505(254 - 2.54S)} \times 10^6, \tag{2.2}$$

where S is the hardness of the material on the Shore A scale and E is the Young's modulus in Pa. Based on this relation, the Young's modulus of the poyurethane is $E_{\text{poly}} = (2.67 \pm 0.14) \times 10^7$ Pa. There is little documentation on the range of Poisson's ratio values for polyurethanes. Using an available range of documented Young's and shear moduli [29], one can obtain Poisson's ratios outside of the physically possible range for a linear elastic material (values from $\nu = -1$ to $\nu = 0.5$ are allowable) [30]. It was assumed that the material is not auxetic, and so simulations were run over a range of Poisson's ratios between 0 and 0.5. The values chosen were ν =0.001, 0.125, 0.250, 0.330, 0.0.350, 0.360, 0.365, 0.370, 0.375, 0.380, 0.390, and 0.400. The appropriate value of ν was later identified based on experimental data.

Simulations were carried out for applied nominal forces from $F_0 = 250$ through 5000 N in increments of 250 N. After each simulation, the vertical dis-

placement of the topmost vertex of the tooth was recorded. This was chosen as the metric because its change should be most closely reflected in the displacement of a clamp, assuming that no tooth climbing occurs. Then, a least squares approach was used to fit lines to the data in order to calculate an effective stiffness for the tooth, as shown in Figure 2.4. This method yielded values for the effective spring constant of the tooth ranging from $k_{\text{tooth}} = 1.86 \times 10^6$ N/m for the $\nu = 0.001$ case to $k_{\text{tooth}} = 6.19 \times 10^6$ N/m for the $\nu = 0.400$ case. In order to model the stiffness of the belt-clamp connection, two tooth stiffnesses were joined in parallel (as shown in Figure 2.2), such that $k_{\text{conn}} = 2k_{\text{tooth}}$. This configuration was chosen in order to incorporate the effect of the first two belt teeth engaged by the clamp. The rest of the teeth were neglected because they carry less of the load [13]. The k_{conn} values were used to calculate the combined spring constant for the connection-belt-connection system illustrated in Figure 2.2 via Eq. (2.1), as discussed in Chapter 5. As is also shown in Chapter 5, $\nu = 0.4$ was found to be the appropriate value for the Poisson's ratio.

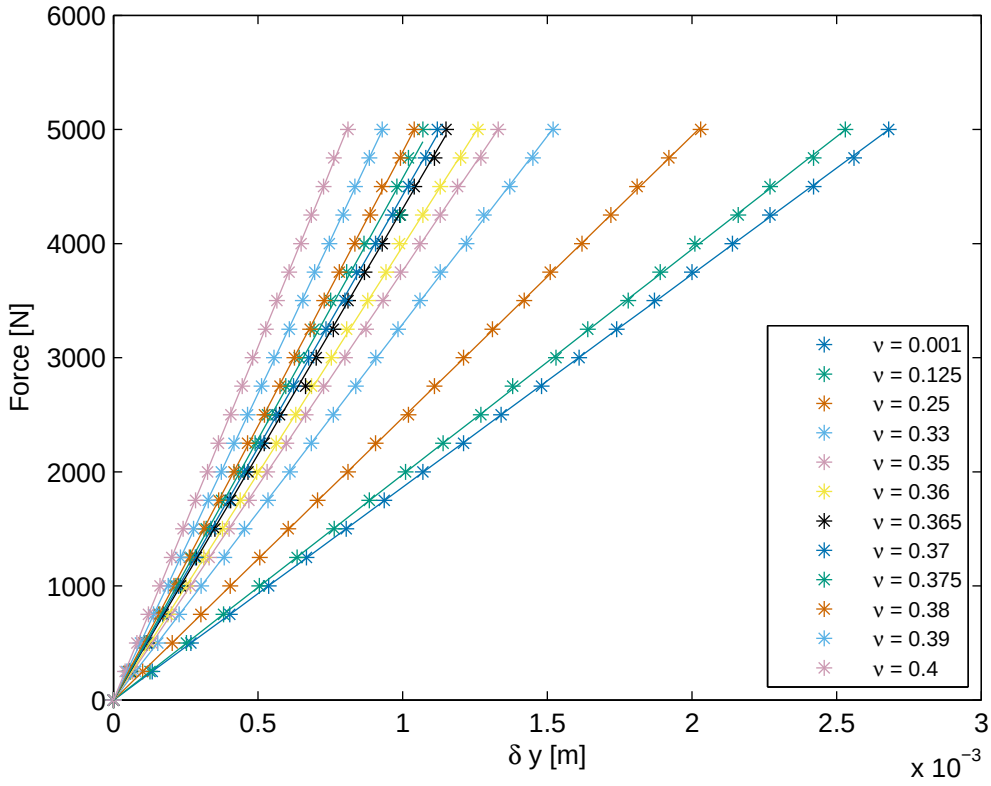

Figure 2.4: The results of the finite element analysis of a single tooth subjected to edge loads. The variable on the horizontal axis, δy, represents absolute value of the vertical displacement of the top vertex of the tooth. The lines are linear fits calculated by a least squares method.

Chapter 3

Experimental Apparatus

3.1 Variables to be Controlled

In order to investigate the validity of acoustic monitoring of the tension in a composite belt, we have created an experimental test apparatus—hereafter referred to as the "Test Stand"—that allows control of the tension in the belt, repeatable impulse excitation of the belt, and acoustic measurement of the resultant vibrations. Before the design of the device is addressed, let us investigate the variables that need to be controlled by the Test Stand. First, consider a string of length L, fixed at both ends, struck at a point x_0 with velocity u_0, as shown in Figure 3.1. The general solution to the vibrating string problem is

$$\xi(x,t) = \sum_{n=1}^{\infty} \sin \frac{n\pi x}{L} [a_n \cos \omega_n t + b_n \sin \omega_n t], \tag{3.1}$$

where ξ is the transverse displacement of the string and n is the mode number [31]. The boundary conditions and initial conditions are described by the following set of expressions

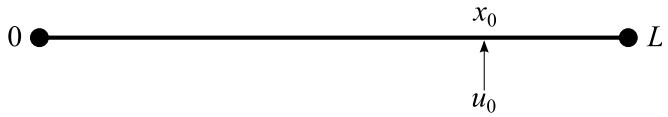

Figure 3.1: A string with fixed boundaries of length L, struck at x_0 with velocity u_0.

$$\xi(0,t) = 0 \qquad \xi(L,t) = 0 \tag{3.2a}$$

$$\xi(x,0) = 0 \qquad \dot{\xi}(x,0) = u_0\delta(x - x_0), \tag{3.2b}$$

where δ is the Dirac delta.

Because initial displacement of the string is zero, the coefficients a_n are zero. The coefficients b_n are given by

$$\begin{aligned} b_n &= \frac{2}{L\omega_n}\int_0^L u_0\delta(x - x_0)\sin\frac{n\pi x}{L}dx \\ &= \frac{2u_0}{n\pi c}\sin\frac{n\pi x_0}{L}, \end{aligned} \tag{3.3}$$

where c is the speed of sound in the string, given by

$$c = \sqrt{T/\rho_\ell}, \tag{3.4}$$

where T is the tension in the string and ρ_ℓ is the mass per unit length—or linear mass density—of the string [31].

From the above, it is clear that the vibration of the string is affected by its length, the location of the excitation, and the tension in the string. Thus, it is important to be able to control each of these variables.

If we extend our view from a 1-dimensional string to a 2-dimensional membrane, then another factor becomes important. A non-uniform tension distribution across the width of the membrane—which, in the case of a power transmission belt drive, can be the result of pulley misalignment—leads to changes in the frequency and modes of vibration of the membrane [32]. Therefore, in addition to controlling the total tension in the belt, we must have control over the tension distribution across the face of the belt.

3.2 Description of Experimental Apparatus

The Test Stand itself is a steel frame consisting of plates on the top and bottom and four vertical support columns, as shown in Figure 3.2. A length of belt was placed in off-the-shelf clamps sold by the belt's manufacturer, which integrate with the teeth of the belt, thus providing a better mechanical connection than would otherwise be possible. By positioning these clamps one at the end of the belt and the other at the desired length, the active vibrating length of the belt was controlled. After the clamps were fastened to the belt, the clamp at the end of the belt was attached to the top plate of the Test Stand with bolts, and the other was inserted into an assembly toward the bottom of the Test Stand that extends horizontally out beyond the vertical support columns.

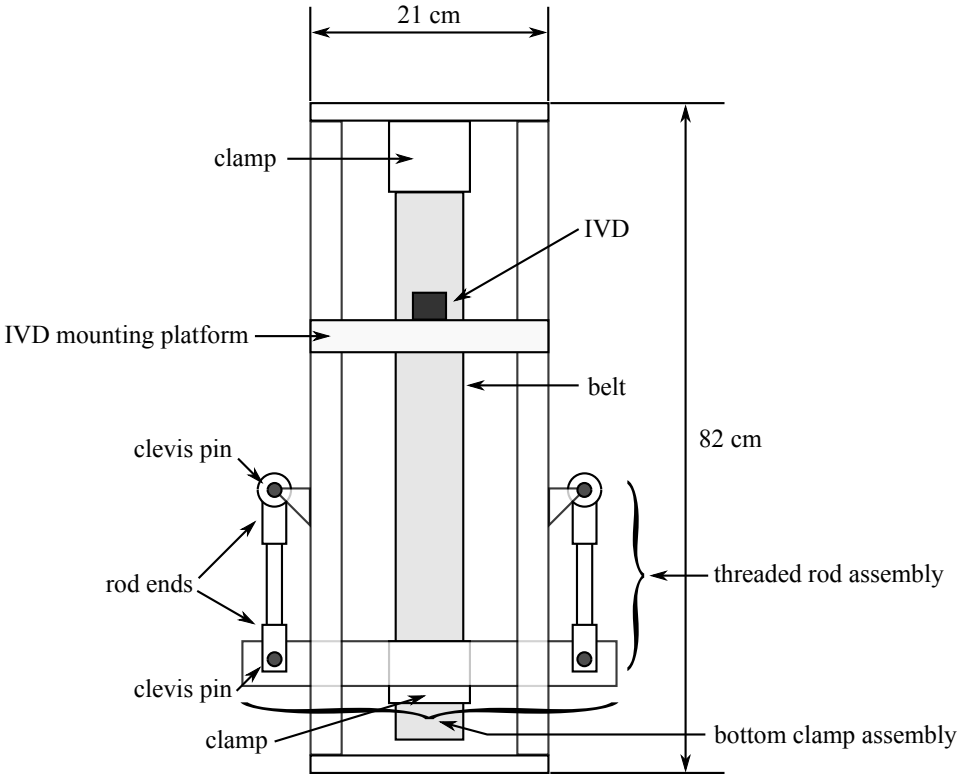

Figure 3.2: A schematic diagram of the experimental apparatus.

Tension was applied to the belt by means of mechanical elongation. The belt was elongated using two turnbuckle-like threaded rods mounted on either side of the Test Stand and attached to the bottom clamp assembly by a pinned connection. These rods are threaded in opposite directions on opposite ends, such that rotating the rod in one direction causes the attached rod ends to move in opposite directions—either closer together or farther apart. By twisting these rods, the bottom clamp assembly can be translated downward, corresponding to elongation of the belt. The displacement was measured by means of two dial indicators (Shars Tool Co. part # 303-3112) in contact with

the bottom clamp assembly near the right and left edges of the belt face. Because the threaded rods are allowed to turn independently, the distribution of tension across the face of the belt can be controlled. By displacing both sides of the bottom clamp assembly equally, the tension across the belt face will be uniform. Deviation from a uniform tension distribution may be obtained by displacing one side farther than the other.

Vibrations were excited in the belt using a custom-designed device consisting of a spring-return solenoid with a rounded plastic tip affixed to the end of its core, that sits upon a movable mounting platform. This device imparts an impulse-like velocity excitation to the flat face of the belt, and is hereafter referred to as the "Initial Velocity Device" (IVD). The mounting platform allows for the IVD's striking head to be positioned almost anywhere with respect to the belt's length and width. The length of time that the solenoid was engaged was regulated by a control circuit and could be specified by the experimenter. The acoustic response of the belt was measured by means of a PCB Piezotronics model U130D20 microphone mounted in a custom bracket attached to the top of the IVD. The model U130D20 is a condenser microphone with a nearly flat frequency response from 20 Hz to 20 kHz [33], which covers the range of frequencies expected in the experiments. The microphone's sensitivity is reported by the manufacturer as 45 mV/Pa [33]. The entirety of the Test Stand was placed on a layer of styrofoam to isolate it from any vibrations from the floor.

Chapter 4

Experimentation

4.1 Simple String Experiment

Before performing experiments with a timing belt, experiments using a steel string were carried out in an effort to validate that the Test Stand operated as expected. The goal of these experiments was to show that the translation of the bottom clamp assembly on the Test Stand is linearly related to the tension experienced by a string fastened in the clamps, and that this relationship could be observed by exciting transverse vibrations in the string and measuring the resulting acoustic signal. A sufficiently long, thin belt under tension is expected to behave as a string to a good approximation [25], with its transverse modes of vibration corresponding to simple string modes. Thus, if the Test Stand did not yield the expected results for a simple string, there would be strong reason to doubt that it would apply tension to the timing belt in the expected manner.

4.1.1 Additional Apparatus

In order to test that the experimental apparatus was working as expected, experiments were performed using a guitar string in place of the belt sample. A 20 gauge (0.020 inch diameter) guitar string made by GHS strings was selected because it was the thickest monofilament string available at the local music store. The string was placed in the clamps using paper shims to replace the thickness of the belt and to protect the clamps. The string was kept from slipping axially by placing the ball end of the string just below the bottom clamp and kinking the free end of the string at the top clamp before the clamp was bolted to the top plate of the Test Stand.

It was quickly discovered that the IVD did a poor job of exciting audible vibrations in the string, so a different configuration of the solenoid was devised, with the goal of applying an initial displacement to the string instead of an initial velocity. The solenoid was turned around so that, when engaged, the core moved away from the center of the Test Stand, rather than toward it. The plastic striking head was removed from the core, and a plastic plectrum was attached to the back of the core using epoxy and vinyl tape. This configuration of the solenoid assembly is hereafter referred to as the "automatic plectrum." The assembly was positioned so that the string was between the plectrum and the coil of the solenoid, such that engaging the solenoid would cause the string to be plucked. The amount of time that the solenoid was engaged was increased so that the solenoid core would be held out of the way of the string while data was recorded.

In this configuration, the bracket to hold the microphone would not fit on the solenoid, so instead, a piece of styrofoam with a hole through its center was attached to the solenoid and the microphone was placed inside. This allowed for the microphone to be positioned easily and also helped to insulate the microphone from Test Stand vibrations.

4.1.2 Procedure

The string was placed in the Test Stand as described above, and then the threaded rods were lengthened by hand until resistance was felt. A bubble level was placed on the bottom clamp assembly to ensure uniform extension of the rods, and then the dial indicators were placed in contact with the bottom clamp assembly and zeroed. The nominal length of the string was $L = 0.525 \pm 0.002$ m. For the experiment, it was elongated from $\delta = 0.000$ inches to $\delta = 0.050$ inches in increments of 0.005 inches, as measured by the dial indicators. Data was taken at the $\delta = 0.000$ inch point to help account for uncertainty in the point of tension onset in the string. The string was plucked sixteen times at each elongation, using the automatic plectrum. For each of these trials, the acoustic data detected by the microphone was recorded using a Tektronix 3014B oscilloscope for 2 seconds at a sampling rate of 5 kHz, triggered to avoid recording the sound caused by the solenoid movement. The data was then transferred from the oscilloscope to a personal computer for processing. Examples of the raw time series data are shown in Section 4.3.1.

4.2 Belt Experiment

4.2.1 Additional Apparatus

For the belt vibration experiment, the IVD was returned to its original state, as described in Section 3.2. That is, the solenoid was turned around and the rounded plastic striking head was again attached to the solenoid's core. The time for which the solenoid was engaged was reduced so that the striking head would not be held in contact with the belt, interfering with vibrations. A belt sample 1 m in length with linear mass density $\rho_\ell = 0.46 \pm 0.02$ kg/m was placed in the clamps and attached to the Test Stand such that its nominal length was $L = 0.524 \pm 0.001$ m. The IVD's mounting platform was positioned horizontally such that the striking head would hit the middle of the belt face in order to avoid exciting torsional modes of vibration. The IVD was positioned vertically to avoid striking a node and thereby failing to excite a particular harmonic frequency. In a second set of experiments, the IVD was placed off-center horizontally, at a position of 5/17 of the width of the belt.

4.2.2 Procedure

As in the simple string experiments, the threaded rods were initially lengthened by hand until there was resistance, and a bubble level was used to ensure that the bottom clamp assembly remained level, indicating uniform translation of the bottom clamp assembly. When resistance was felt, the dial indicators were placed in contact with the bottom clamp assembly, near the left and right edges of the belt face, and zeroed. For both sets of experiments,

the belt was elongated from $\delta = 0.010$ inches to $\delta = 0.050$ inches in 0.005 inch increments. Vibrations were excited using the IVD, and, as before, the acoustic data deteced by the microphone was recorded by the oscilloscope for 2 seconds at a sampling rate of 5 kHz, triggered appropriately to avoid recording the sound of the solenoid's motion. As in the simple string experiments, sixteen trials were taken at each elongation.

4.3 Data Processing

4.3.1 Examples of Raw Data

The waveforms detected by the microphone and sampled by the oscilloscope were transferred to a personal computer where they could easily be used for calculations. An example of the acoustic data for the simple string experiments described in Section 4.1 is shown in Figure 4.1. The data in that example was obtained in the fourteenth trial of the $\delta = 0.015$ inch elongation in the first of the two simple string experiments. This data is used in all of the examples regarding the simple string experiments in this section.

A spectrogram of the data offers further insight into how the string is vibrating and how to approach processing. A Short-Time Fourier Transform (STFT) of the data was taken using a 256-point Hamming window. The resulting spectrogram is shown in Figure 4.2. There are many frequency peaks in the signal, as expected, because the string was initially displaced so that its shape approximated a triangle. That is, the initial waveform inherently contains rich harmonic frequency content because a triangular pulse can be

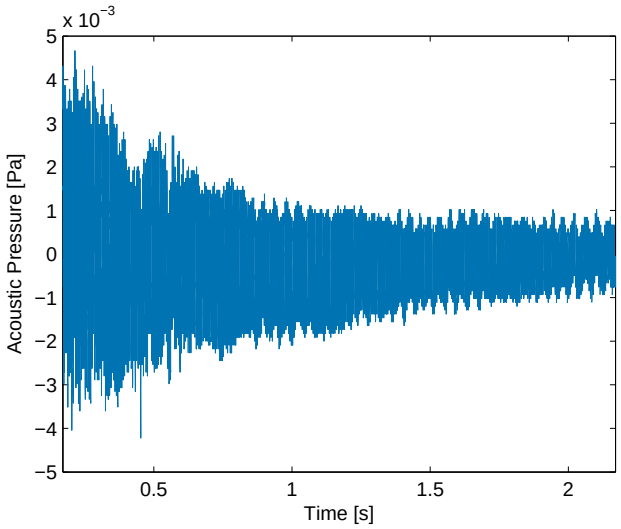

Figure 4.1: An example of the time series data collected in the simple string experiments. This data was taken during the fourteenth trial for the $\delta = 0.015$ inch elongation in the first of the two simple string experiments.

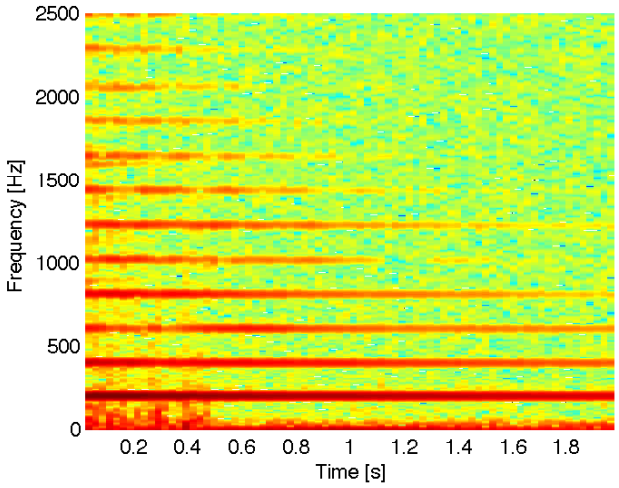

Figure 4.2: A spectrogram of the time series data shown in Figure 4.1 (simple string). The Short-Time Fourier Transform (STFT) was carried out using a Hamming window of length 256.

constructed with an infinite sum of harmonic sinusoids. By inspection, the peaks appear to be evenly spaced, indicating that they are harmonics. At the beginning of the time interval, there are peaks that do not seem to fall into the harmonic structure, but these appear to die out within about 0.5 seconds. The strongest peaks appear to be the first four, as they are visible for the entire time interval.

The data from the belt vibration experiment is now similarly shown. The acoustic pressure data for the first trial of the $\delta = 0.025$ inch elongation of the first belt experiment is shown in Figure 4.3. Similar data for the eleventh trial of the $\delta = 0.025$ inch elongation of the third repetition of the second belt experiment is shown in Figure 4.4. Notice that there appears to be some low frequency beating (amplitude modulation) present in the signal for both experiments, and it is more pronounced in the data from the experiment with the IVD off-center.

Using the same window as before, spectrograms of these data sets were created—see Figure 4.5 and Figure 4.6. There is essentially no energy above 500 Hz in the signals, so no frequencies beyond this are shown in the spectrograms. It is clear that there are only four significant frequency peaks in these signals and that they occur at roughly the same frequencies in each, as expected. There is low-frequency energy spread across the entire time interval, which may be associated with the beating that is visible in Figure 4.3 and Figure 4.4.

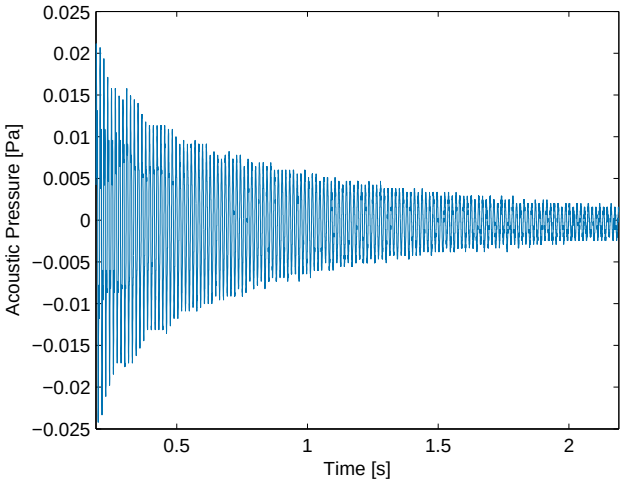

Figure 4.3: An example of the time series data collected in the belt vibration experiment with the IVD centered on the belt face. This data was taken during the first trial for the $\delta = 0.025$ inch elongation.

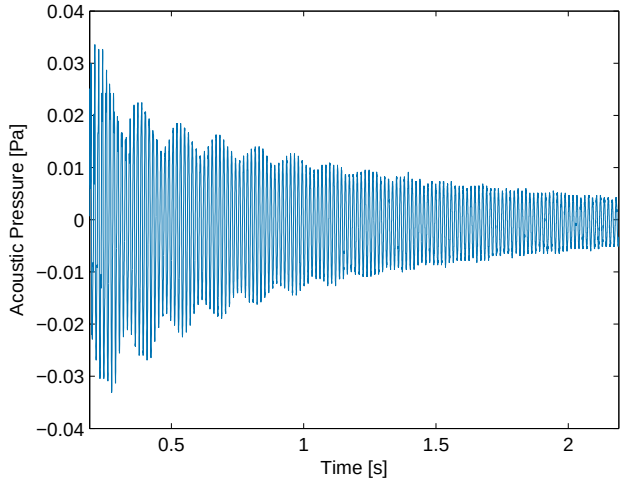

Figure 4.4: An example of the time series data collected in the belt vibration experiment with the IVD positioned at 5/17 of the width of the belt face. This data was taken during the eleventh trial for the $\delta = 0.025$ inch elongation in the third repetition of the experiment.

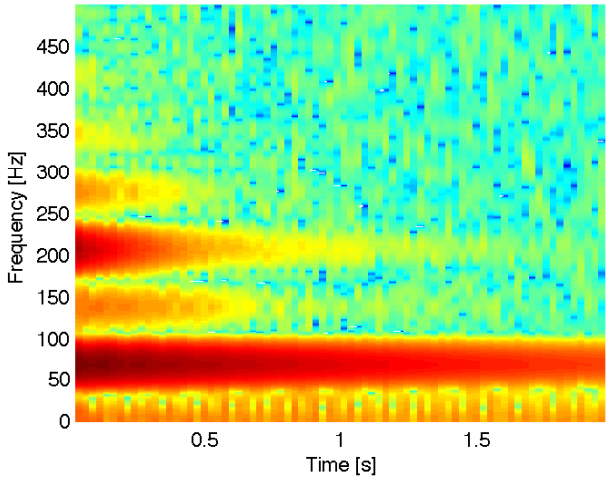

Figure 4.5: A spectrogram of the time series data shown in Figure 4.3 (timing belt excited on center). The STFT was carried out using a Hamming window of length 256. Only frequencies up to 500 Hz are shown because there are no interesting features above this frequency.

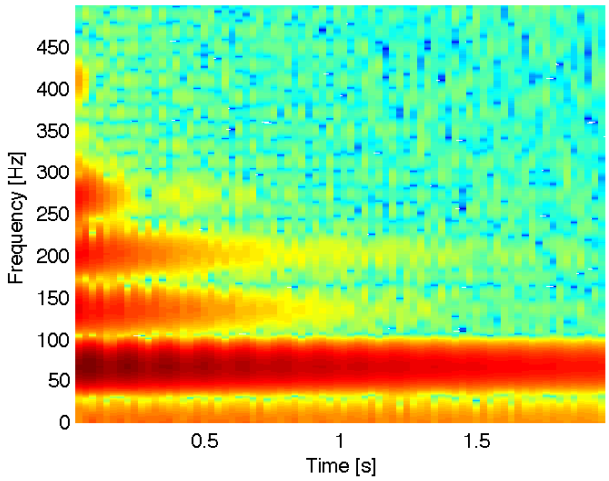

Figure 4.6: A spectrogram of the time series data shown in Figure 4.4 (timing belt excited off-center). The STFT was carried out using a Hamming window of length 256. Only frequencies up to 500 Hz are shown because there are no interesting features above this frequency.

4.3.2 Processing Algorithm

The method of processing the data to yield tension estimates was essentially the same for both types of experiment. First, the frequency spectra of the time series data were calculated using a Fast Fourier Transform (FFT). Then, the first four modal frequencies were extracted from the spectra using a peak finding algorithm. The results of the peak finding algorithm were visually inspected and any errors were corrected by modifying the algorithm's input parameters such as the mininmum peak height and the minimum distance between peaks. Figures 4.7 and 4.8 show examples of the frequency spectra of the data from the simple string and belt experiments, respectively, with the first four modal frequencies marked. In Figure 4.8, note the smaller, secondary peaks that are visible in the FFT of the data from the belt vibration experiment with the IVD placed off-center (the red curve). It is speculated that these may be evidence of torsional vibration of the belt or structural vibrations of the Test Stand, but a thorough investigation is beyond the scope of this thesis.

After the modal frequencies were determined, the effective sound speed in the material was calculated using a relationship that is valid for a vibrating string; namely,

$$f_n = \frac{nc}{2(L+\delta)}, \tag{4.1}$$

where f_n is the frequency of the n^{th} mode, L is the equilibrium length of

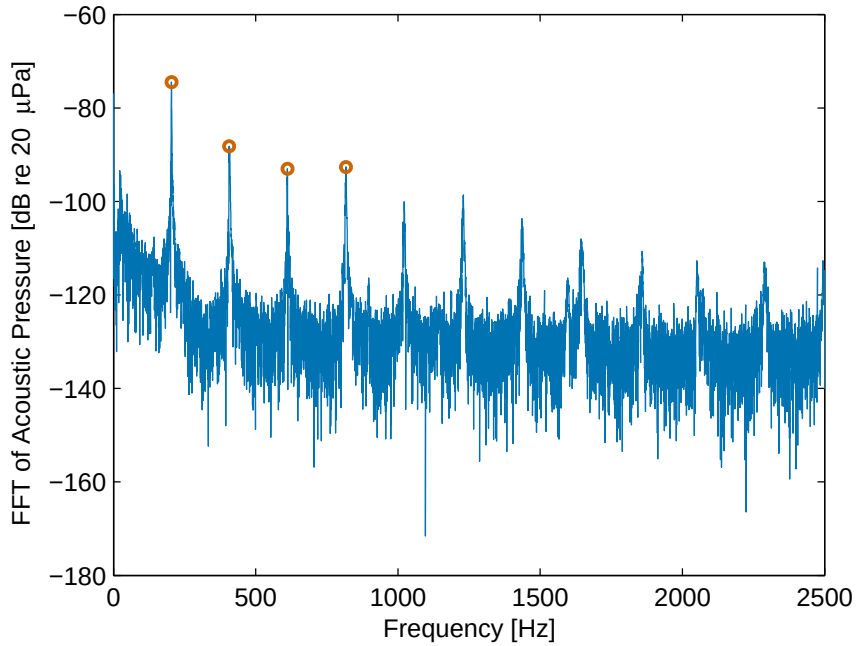

Figure 4.7: The Fast Fourier Transform (FFT) of the data shown in Figure 4.1 (simple string). The first four harmonic frequencies are marked by the circles.

the string, and δ is the extension beyond the equilibrium length. Specifically, least squares linear fits of modal frequency with respect to mode number were performed for all data sets, and the resulting slopes were multiplied by $2(L + \delta)$ to obtain values for the effective sound speed, c. Then, the tension was calculated by rearranging Eq. (3.4) to obtain

$$T = \rho_\ell c^2. \tag{4.2}$$

After tension values were calculated for every δ and every trial of an experiment, a line was fit to the entire data set, using a least squares method. The

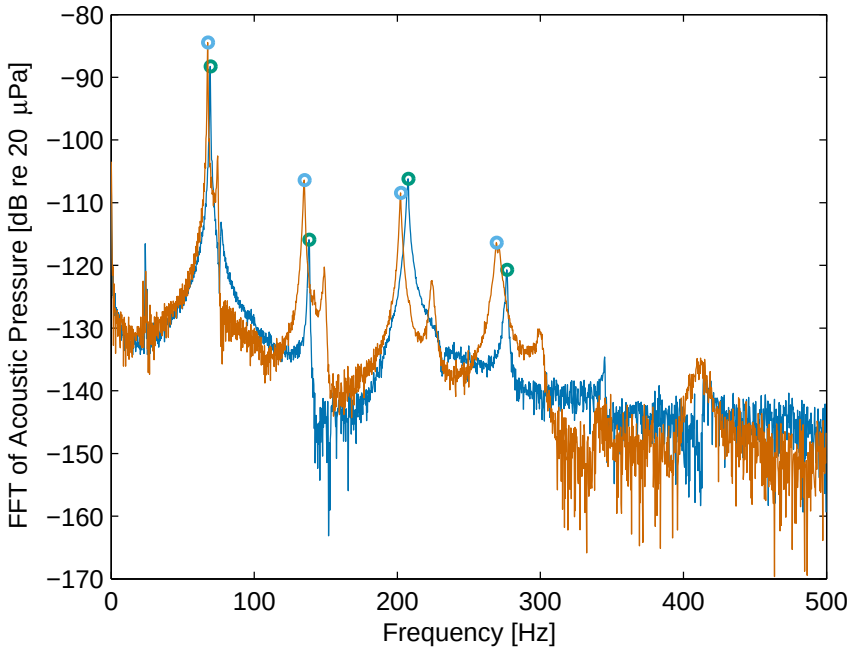

Figure 4.8: The FFTs of the timing belt data shown in Figure 4.3 (on-center excitation, blue) and Figure 4.4 (off-center excitation, red). The first four harmonic frequencies are marked by the circles.

slope of the line can be considered an effective stiffness for the material. The slope and intercept from this linear fit were then used to compute an offset in δ to correct for uncertainties in the location of $\delta = 0$, where tension is first experienced by the string or the belt, and to aid in model computations.

The quantities used in the calculations each have an associated uncertainty, which will be denoted by $u(q)$, where q is the quantity. The uncertainty in the extension was taken to be $u(\delta) = 0.001$ inches, which is twice the least count of the dial indicators. Note that $u(L)$ and $u(\rho_\ell)$ are not the same for the simple string and belt experiments, and thus they will be pre-

sented with the results of the experiments in Section 4.4. The uncertainty in the modal frequencies was taken to be one half of the frequency increment in the FFT, which is 0.3052 Hz in this case, so the uncertainty in the modal frequencies is $u(f_n) = 0.1526$ Hz. The least-squares estimate of the slope of the f_n vs. n line, which will be referred to as f_0 because it assumes the role of the fundamental frequency, has an error based on the propagation of $u(f_n)$ through the least squares calculation. In general, given a set of data $(x_1, y_1), (x_2, y_2), \ldots, (x_N, y_N)$, the slope of the line $y_n = mx_n + c$, as estimated by a least squares approach [34], is given by the formula

$$m = \frac{N\sum_{n=1}^{N} x_n y_n - \sum_{n=1}^{N} x_n \sum_{n=1}^{N} y_n}{N\sum_{n=1}^{N} x_n^2 - \left(\sum_{n=1}^{N} x_n\right)^2}. \tag{4.3}$$

Substituting the appropriate values for our particular case—$m = f_0$, $N = 4$, $x_n = n$, and $y_n = f_n$—we have

$$f_0 = \frac{1}{5}\sum_{n=1}^{4} n f_n - \frac{1}{2}\sum_{n=1}^{4} f_n. \tag{4.4}$$

The general formula for the propagation of uncertainty is

$$u(R) = \sqrt{\left[u(q_1)\frac{\partial R}{\partial q_1}\right]^2 + \left[u(q_2)\frac{\partial R}{\partial q_2}\right]^2 + \ldots + \left[u(q_N)\frac{\partial R}{\partial q_N}\right]^2}, \tag{4.5}$$

where $R = R(q_1, q_2, \ldots, q_N)$. Applying Eq. (4.5) to Eq. (4.4) yields

$$u(f_0) = \frac{u(f_n)\sqrt{5}}{5}, \tag{4.6}$$

which evaluates to $u(f_0) = 0.0682$. Using Eq. (4.5), the uncertainty in the effective sound speed, $c = 2(L + \delta)f_0$, is given by

$$\begin{aligned} u(c) &= \sqrt{\left[u(L)\frac{\partial c}{\partial L}\right]^2 + \left[u(\delta)\frac{\partial c}{\partial \delta}\right]^2 + \left[u(f_0)\frac{\partial c}{\partial f_0}\right]^2} \\ &= \sqrt{\big(u(L)f_0\big)^2 + \big(u(\delta)f_0\big)^2 + \big(u(f_0)(L+\delta)\big)^2} \\ &= |c|\sqrt{\left[\frac{u(L)}{L+\delta}\right]^2 + \left[\frac{u(\delta)}{L+\delta}\right]^2 + \left[\frac{u(f_0)}{f_0}\right]^2}. \end{aligned} \tag{4.7}$$

Lastly, the uncertainty in the experimentally measured tension can be computed by

$$\begin{aligned} u(T) &= \sqrt{c^4\big(u(\rho_\ell)\big)^2 + 4\rho_\ell^2 c^2\big(u(c)\big)^2} \\ &= |T|\sqrt{\left[\frac{u(\rho_\ell)}{\rho_\ell}\right]^2 + \left[\frac{2u(c)}{c}\right]^2}. \end{aligned} \tag{4.8}$$

The experimental results and their uncertainties are reported in the following section.

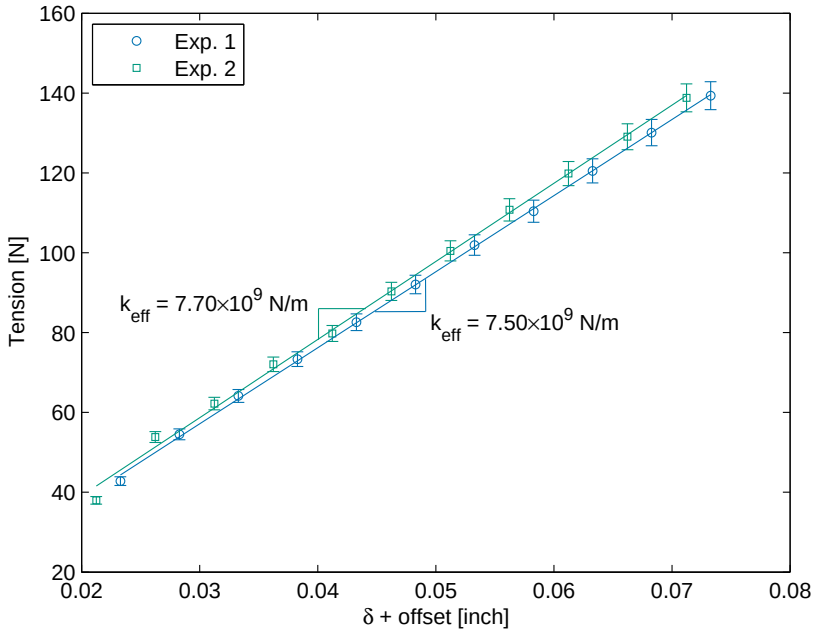

Figure 4.9: Measured tensions from the simple string experiments. The mean values are shown. The δ offsets are 0.023 inches for the first experiment, and 0.021 inches for the second. Error bars were obtained by propagating the uncertainties in each measured value through the calculation of the mean according to Eq. (4.5). The linear fits were calculated using a least squares method and the resulting effective stiffnesses are shown on the plot.

4.4 Results

4.4.1 String

For the simple string experiments, the following parameters were used. The density of the steel was taken to be $\rho = (7.85 \pm 0.01) \times 10^3$ kg/m^3 [35], the string's length was $L = 0.525 \pm 0.002$ m, and its diameter was $D = 0.0200 \pm 0.0005$ inches. The linear mass density was calculated to be $\rho_\ell = (1.58 \pm 0.08) \times 10^{-3}$ kg/m. The results of the simple string experiments are shown in

Figure 4.9. The effective stiffnesses calculated were $(7.50 \pm 0.09) \times 10^4$ N/m and $(7.70 \pm 0.09) \times 10^4$ N/m for the first and second experiments, respectively. The δ offsets were 0.023 and 0.021 inches, respectively. From Figure 4.9, it can be seen that there is agreement between the linear fits that yield the effective stiffness values and the mean measured tension values, within their 95% confidence intervals.

4.4.2 Belt

For the belt experiments, the following parameters were used. The linear mass density of the belt was taken to be $\rho_\ell = 0.46 \pm 0.02$ kg/m and the belt's length was $L = 0.524 \pm 0.001$ m. The experimental results are shown in Figure 4.10 and Figure 4.11. The δ offset for the on-center excitation experiment was calculated to be 0.005 inches. The effective stiffness was calculated to be $(3.19 \pm 0.04) \times 10^6$ N/m, which agrees with the means of the measured tension values, within their 95% confidence intervals, as can be seen in Figure 4.10. For the experiment with the IVD positioned off-center, the δ offsets were calculated to be 0.005, 0.004, 0.004, and 0.005 inches for the four runs, respectively. The least squares linear fits resulted in effective stiffnesses of $(2.85 \pm 0.03) \times 10^6$ N/m, $(3.03 \pm 0.04) \times 10^6$ N/m, $(3.20 \pm 0.04) \times 10^6$ N/m, and $(3.25 \pm 0.04) \times 10^6$ N/m, respectively. All of the calculated effective stiffnesses are consistent with the data within the 95% confidence intervals of the means of the particular experiments.

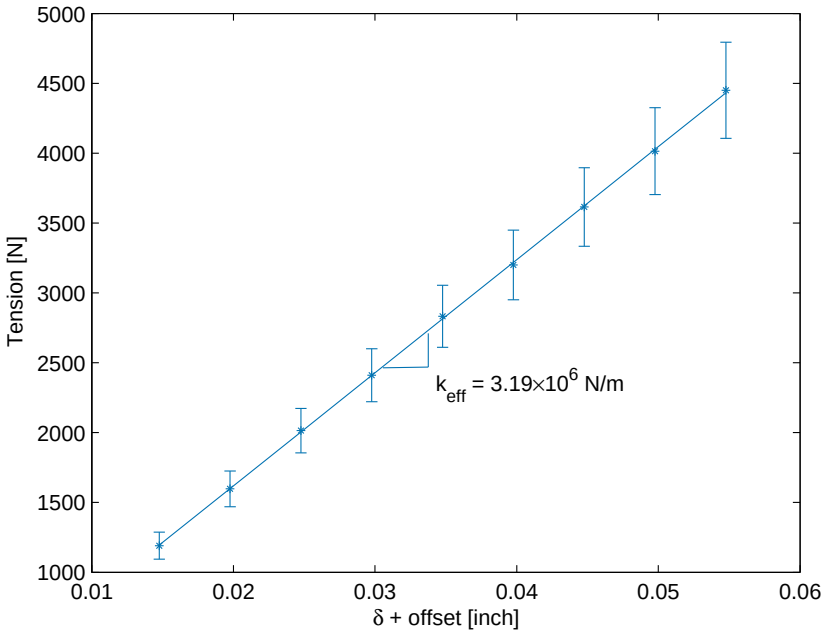

Figure 4.10: Measured from the belt vibration experiment with the IVD centered on the belt face. The mean values are shown. The δ offset is approximately 0.005 inches. Error bars were obtained by propagating the uncertainties in each measured value through the calculation of the mean according to Eq. (4.5). The linear fit was calculated by a least squares method and the resulting effective stiffness is shown on the plot.

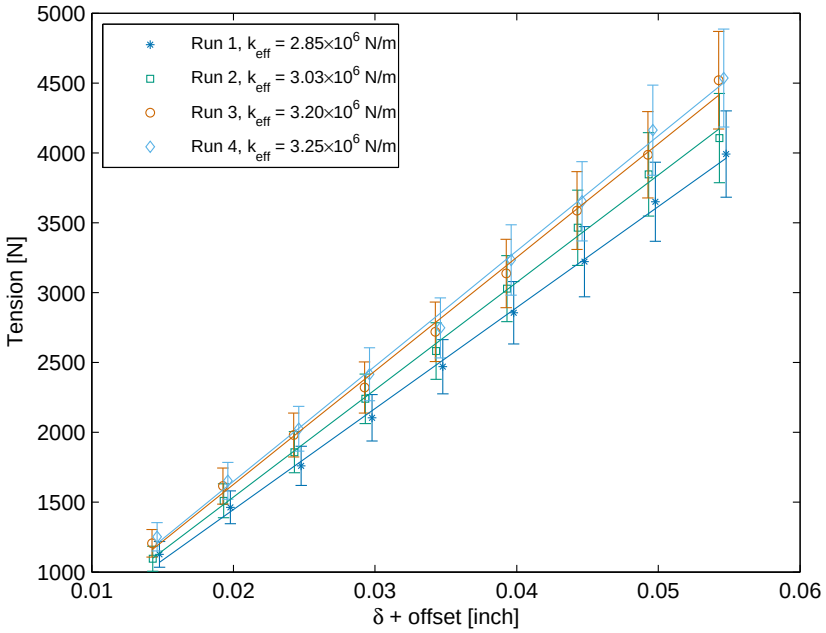

Figure 4.11: The mean values of the measured tensions from the belt vibration experiments with the IVD positioned at 5/17 of the width of the belt face. The δ offsets are approximately 0.005, 0.004, 0.004, and 0.005 inches, respectively. Error bars were obtained by propagating the uncertainties in each measured value through the calculation of the mean according to Eq. (4.5). The linear fits were calculated by a least squares method and the resulting effective stiffnesses appear in the legend.

Chapter 5

Comparison of Measurements to Models

5.1 String Experiment

In order to make meaningful comparisons between the predictions of the models and the experimental data, it was necessary to calculate uncertainties for the models, just as had been done for the experimental values. The simple string is expected to carry tension as an effective spring according to Hooke's law. From

$$T = \frac{AE}{L}\delta, \tag{5.1}$$

we can calculate the effective spring constant of the string, with parameters described in Section 4.1, to be $k_{\text{st}} = AE/L = (7.9 \pm 0.4) \times 10^3$ N/m [36]. The uncertainty in this value was found by using Eq. (4.5) to propagate uncertainties in the string's diameter and length, $u(D) = 0.0005$ inches and $u(L) = 0.002$ m, as well as in the Young's modulus of steel, $u(E_{\text{st}}) = 5 \times 10^9$ Pa [35, 37], through the calculation of Eq. (5.1). To obtain tension values, T_{mod}, this effective spring constant was then multiplied by the sum of the elongation of the spring and the calculated offset discussed in Section 4.3.2. By applying Eq. (4.5) and ignoring any uncertainty associated with the offset, the uncertainty in the model

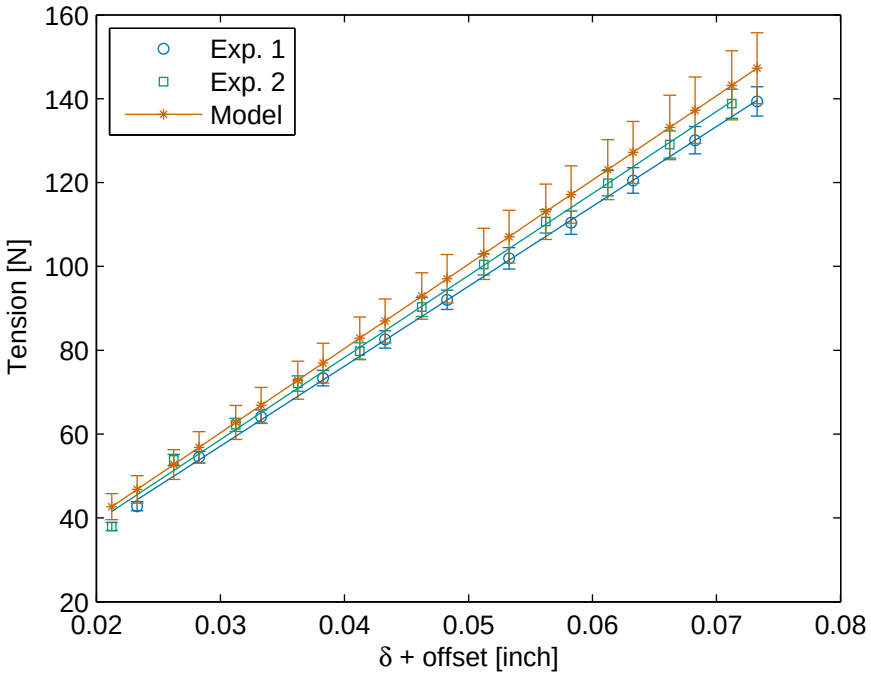

Figure 5.1: The results of the simple string experiment with predictions based on an effective spring model.

tension values was found to be given by the expression

$$u(T_{\text{mod}}) = |T_{\text{mod}}| \sqrt{\left[\frac{u(k_{\text{st}})}{k_{\text{st}}}\right]^2 + \left[\frac{u(\delta)}{\delta}\right]^2}. \tag{5.2}$$

The results of the experiment, along with the predictions of this model are shown in Figure 5.1. The model is consistent with the measurements within the 95% confidence intervals, except for the $\delta = 0$ point of the second experiment. These results indicate that the Test Stand is working as intended.

5.2 Belt Experiment

For the belt vibration experiment, it was necessary to calculate uncertainties for the manufacturer's model and the model incorporating tooth stiffness. Uncertainty was incorporated into the manufacturer's model by using the uncertainty implicit in the tabulated value for the specific belt stiffness. Because the value is reported as $k_{\text{spec}} = 4.25 \times 10^5$ N/10 mm of belt width, it can be inferred that there is an uncertainty of $u(k_{\text{spec}}) = 4 \times 10^2$ N/10 mm of belt width. Using this value along with an uncertainty in the belt width of $u(w) = 1$ mm and $u(L) = 1$ mm as before, the uncertainty in the stiffness of the belt is

$$u(k_{\text{belt}}) = |k_{\text{belt}}| \sqrt{\left[\frac{u(k_{\text{spec}})}{k_{\text{spec}}}\right]^2 + \left[\frac{u(w)}{w}\right]^2 + \left[\frac{u(L)}{L}\right]^2}, \tag{5.3}$$

and the uncertainty in the tension prediction based on this model is

$$u(T_{\text{spr}}) = |T_{\text{spr}}| \sqrt{\left[\frac{u(k_{\text{belt}})}{k_{\text{belt}}}\right]^2 + \left[\frac{u(\delta)}{\delta'}\right]^2}, \tag{5.4}$$

where δ' is δ plus the calculated offset. Thus, according to Eq. (5.3), the belt's stiffness as suggested by the manufacturer is $k_{\text{belt}} = (6.08 \pm 0.08) \times 10^6$ N/m.

The uncertainty in the model incorporating tooth stiffness was calculated in a slightly different way. First, an uncertainty in the reported hardness of the polyurethane, $u(S) = 0.4$ Shore A, was determined in the same way that the uncertainty in the specific belt stiffness had been. Then, this uncertainty was propagated through Eq. (2.2) according to Eq. (4.5), yielding

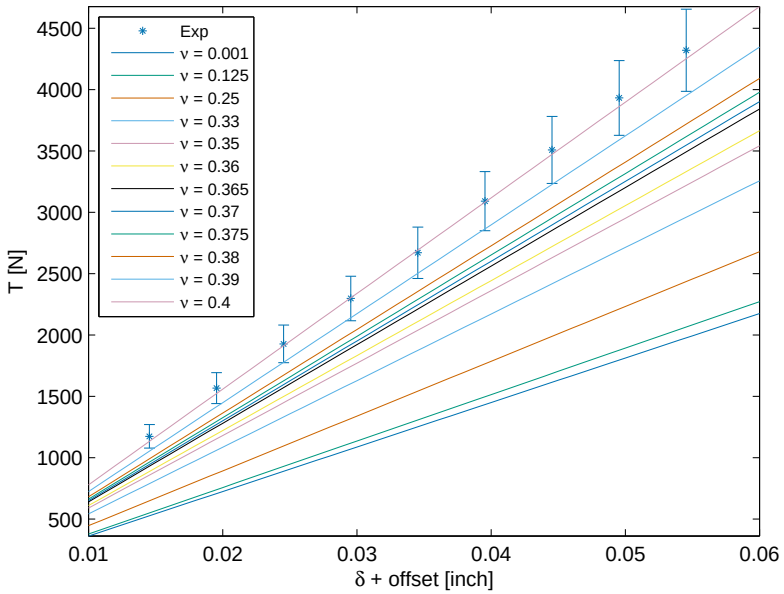

Figure 5.2: Comparison of the means of the measured tensions from all belt experiments, both on- and off-center to the predictions based on the finite element method simulation. The line corresponding to $\nu = 0.4$ is most consistent with the experimental data.

an uncertainty in the Young's modulus of $u(E_{\text{poly}}) = 1.4 \times 10^6$ Pa. This was used to identify high and low values of E_{poly} that were then used in the finite element model in order to find upper and lower bounds on the results of the simulations. So, for each value of ν, the simulation would return a set of three displacements at each F_0, resulting in three different effective spring constants and thus three different tension predictions corresponding to the estimated value and its upper and lower confidence bounds. In order to identify the Poisson's ratio that best reflected the experimental data, the mean tension values—using data from both experiments—were compared to the predictions

of the finite element method simulations, as shown in Figure 5.2. The simulation based on a Poisson's ratio of $\nu = 0.4$—which yields a tooth stiffness of $k_{\text{tooth}} = 6.19 \times 10^6$ N/m and thus, via Eq. (2.1) and $k_{\text{conn}} = 2k_{\text{tooth}}$, an effective stiffness of $k_{\text{eff}} = 3.07 \times 10^6$ N/m—was found to give the best agreement with the experimental data, as the predicted tensions resulting from this model fell within the 95% confidence intervals of the means of the experimental data. This value of ν seems physically reasonable because it falls between the widely accepted values of the Poisson's ratio of steel (0.3) and that of rubber (0.5) [30].

The results of the experiment with the IVD centered are presented with predictions from the models in Figure 5.3. The manufacturer's suggested effective spring model is not consistent with the data. It is clear from Figure 5.3 that the experimental data and the prediction of the improved model—which accounts for the stiffness of the belt-clamp connection using an experimentally inferred value of 0.4 for the Poisson's ratio of polyurethane—agree within their uncertainty bounds. This model is also consistent with the data from the experiments in which the IVD was positioned off-center on the belt face, within the confidence intervals, as shown in Figure 5.4.

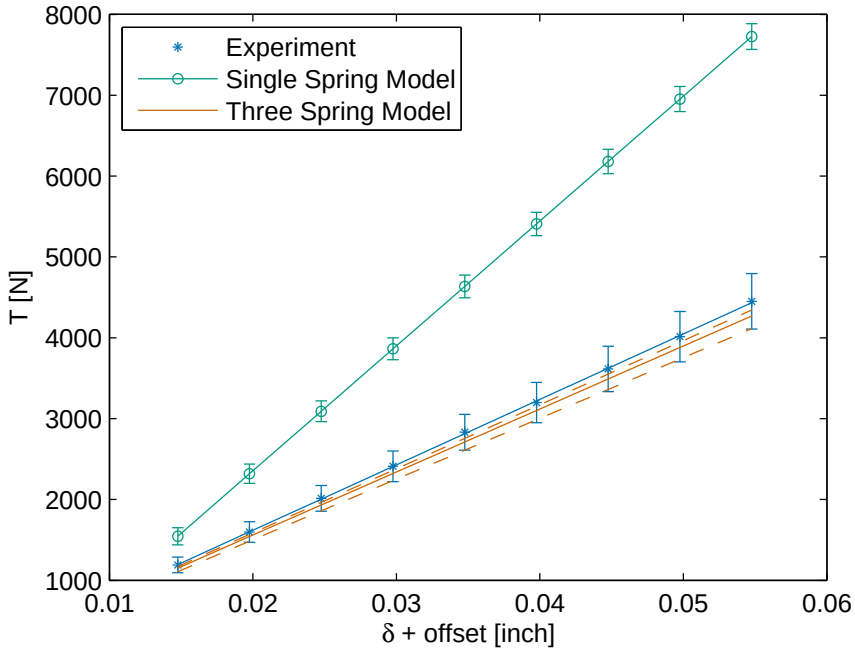

Figure 5.3: The results of the belt vibration experiment with the IVD centered (blue) compared to predictions based on the manufacturer's single spring model (green) and the three spring model with tooth stiffness included (red), using an experimentally-identified Poisson's ratio of $\nu = 0.4$ for the polyurethane. The dashed lines indicate the upper and lower confidence limits on the model.

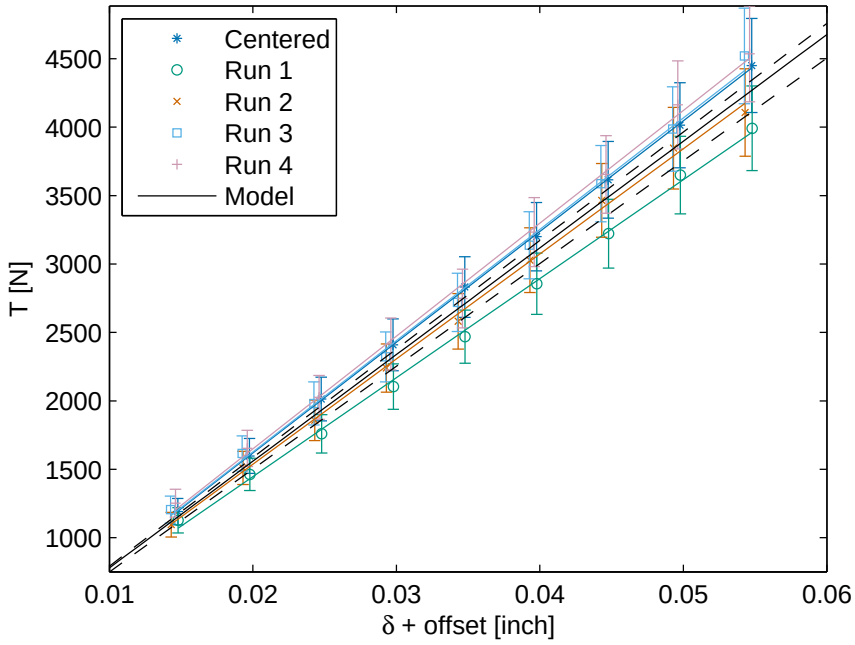

Figure 5.4: The results of the both belt vibration experiments compared to predictions based on the model with tooth stiffness included, using a Poisson's ratio of $\nu = 0.4$ for the polyurethane. The dashed lines indicate the upper and lower confidence limits on the model.

Chapter 6

Conclusions and Future Work

6.1 Conclusions

In this thesis, a lumped-parameter model was developed for tension prediction in a composite timing belt that improves upon the model suggested by the belt manufacturer. In particular, the effects of the geometric complexity of the belt's construction were taken into consideration. The stiffness of a belt tooth was determined by using a finite element model that simulated the deformation of a single polyurethane tooth subjected to forces on two of its faces over a range of values for the Poisson's ratio. The clamped belt system was modeled as three springs connected in series—one corresponding to the belt stiffness suggested by the manufacturer and two representing the stiffnesses of the belt-clamp connections. Each of the stiffness elements due to the belt-clamp connection were modeled as two springs in parallel corresponding to two belt teeth, each with stiffness k_{tooth} as calculated by the finite element model.

Experiments were performed on an apparatus designed to allow control of the length and tension of a belt sample and to repeatably excite transverse vibrations. Acoustic signals were recorded and spectral analysis techniques

were used to calculate the tension in the belt based on the one-dimensional wave equation. The operation of the apparatus was verified by experiments with a simple string, which showed that a linear translation of the bottom clamp assembly of the Test Stand corresponds to a linear increase in the tension in the clamped string. Two types of belt vibration experiment were performed, varying the excitation location. The manufacturer's model was shown to be inconsistent with the experimental data. The tension predictions from the model incorporating the connection stiffness based on teeth with a Poisson's ratio of $\nu = 0.4$ were found to fall within the 95% confidence intervals of the means of the measured tensions from the belt vibration experiments. While this value was identified based on the experimental data, it appears reasonable because it falls between the Poisson's ratios of steel and rubber.

This work has shown that a three spring model of a composite belt results in a significant improvement over the single spring model suggested by the belt's manufacturer. Furthermore, the results of the experiments have shown that the tension in a timing belt consisting of braided steel cables embedded in polyurethane can be measured repeatably by analyzing the frequency spectra of acoustic pressure radiation signals resulting from transverse vibrations.

6.2 Future Work

The foundation has been laid for further experiments to be performed with the experimental apparatus described in this thesis. In particular, preparations have been made to attach force sensors to the Test Stand. This will

allow for the tension in the belt to be measured directly, which will provide another method of testing the validity of the model presented in this thesis. Furthermore, these sensors would facilitate experiments with non-uniform distributions of tension across the face of the belt, which would offer insight into the sensitivity of the model to pulley misalignment.

For further research, the finite element model should be reexamined, as some unexpected behavior was observed. An additional force could be added to the face on the tip of the tooth and the choice of displacement metric could be improved. The next step in refining the model would be to verify the Poisson's ratio of the belt's polyurethane matrix by measurement. Additionally, the finite element model could be extended to include the tension members, or perhaps to model the entirety of the belt span. This could allow the experimenter to break away from the one-dimensional wave equation and investigate more complex vibration phenomena.

Bibliography

[1] USPS. 2001 comprehensive statement on postal operations. `http://about.usps.com/strategic-planning/cs01/c2f-4.htm`, 2001. Date accessed: August 2011.

[2] Daifuku America Corporation. Daifuku material handling and beyond. `http://www.daifukuamerica.com/case_studies/`, 2008. Date accessed: August 2011.

[3] T. Feare. The world's top 20 system suppliers. *Modern Materials Handling*, 55(2):68, 2000.

[4] L. K. Rogers. Top 20 systems suppliers. *Modern Materials Handling*, 64(4):23 – 24, 2009.

[5] G.K. Agrawal and S.S. Heragu. A survey of automated material handling systems in 300-mm semiconductor fabs. *Semiconductor Manufacturing, IEEE Transactions on*, 19(1):112 – 120, February 2006.

[6] Brecoflex Co. L.L.C. Polyurethane timing belts (catalog). `http://brecoflex.com/download/b\_212\_sept2008.pdf`, 2008. Date accessed: February 2010.

[7] J. N. Fawcett. Chain and Belt Drives - A Review. *Shock and Vibration Digest*, 13(5):5–12, 1981.

[8] J. N. Fawcett, J. S. Burdess, and J. R. Hewit. Belt natural frequency as an indicator of belt tension. *Proceedings of 1989 International Conference on Power Transmission and Gearing*, pages 25–29, 1989.

[9] Gates Corporation. Synchronous belt failure analysis guide. `http://www.gatesprograms.com/assets/ptsavings/Belt_Failure_Analysis.pdf`. Date accessed: January 2011.

[10] M.W. Musselman. Improvement of belt tension monitoring in a belt-driven automated material handling system. Master's thesis, The University of Texas at Austin, 2010.

[11] D.A. Melas, I.A. Craighead, and I.I. Esat. An experimental study for measuring the natural frequency of the timing belt. *International Journal of Vehicle Design*, 35(3):274–288, 2004.

[12] R.N. Capps. Dynamic Young's moduli of some commercially available polyurethanes. *The Journal of the Acoustical Society of America*, 73:2000, 1983.

[13] G. Gerbert, H. Jönsson, U. Persson, and G. Stensson. Load distribution in timing belts. *Transactions-American Society of Mechanical Engineers Journal of Mechanical Design*, 100:208–215, 1978.

[14] T.C. Firbank. Mechanics of the belt drive. *International Journal of Mechanical Sciences*, 12(12):1053–1063, 1970.

[15] O. Reynolds. Creep theory of belt drive mechanics. *Engineer*, 38:396–397, 1874.

[16] D.G. Alciatore and A.E. Traver. Multipulley belt drive mechanics: creep theory vs shear theory. *Transactions-American Society of Mechanical Engineers Journal of Mechanical Design*, 117:506–511, 1995.

[17] X. Li and L. Chen. Modal analysis of coupled vibration of belt drive systems. *Applied Mathematics and Mechanics*, 29(1):9–13, 2008.

[18] R.S. Beikmann, N.C. Perkins, and A.G. Ulsoy. Free vibration of serpentine belt drive systems. *Journal of Vibration and Acoustics*, 118:406, 1996.

[19] R.G. Parker. Efficient eigensolution, dynamic response, and eigensensitivity of serpentine belt drives. *Journal of Sound and Vibration*, 270(1-2):15–38, 2004.

[20] L. Zhang and J.W. Zu. Non-linear vibrations of viscoelastic moving belts, part I: free vibration analysis. *Journal of Sound and Vibration*, 216(1):75–91, 1998.

[21] M.J. Leamy and T.M. Wasfy. Analysis of belt-driven mechanics using a creep-rate-dependent friction law. *Journal of Applied Mechanics*, 69:763, 2002.

[22] M.J. Leamy and T.M. Wasfy. Time-accurate finite element modelling of the transient, steady-state, and frequency responses of serpentine and

timing belt-drives. *International Journal of Vehicle Design*, 39(3):272–297, 2005.

[23] G. Čepon and M. Boltežar. Dynamics of a belt-drive system using a linear complementarity problem for the belt-pulley contact description. *Journal of Sound and Vibration*, 319(3-5):1019–1035, 2009.

[24] M. Callegari, F. Cannella, and G. Ferri. Multi-body modelling of timing belt dynamics. *Proceedings of the Institution of Mechanical Engineers, Part K: Journal of Multi-body Dynamics*, 217(1):63–75, 2003.

[25] S. Abrate. Vibrations of belts and belt drives. *Mechanism and Machine Theory*, 27(6):645–659, 1992.

[26] G. Gerbert. Tooth action in chain and timing belt drives. In *Proceedings of the 1989 International Power Transmission and Gearing Conference, ASME*, pages 81–89, 1989.

[27] Onda Corporation. Acoustic properties of rubbers. `http://www.ondacorp.com/images/Rubbers.pdf`. Date accessed: August 2011.

[28] A.N. Gent. On the relation between indentation hardness and Young's modulus. *Rubber Chemistry and Technology*, 31:896, 1958.

[29] MatWeb L.L.C. Overview of materials for thermoplastic polyurethane, elastomer, polyester grade. `http://www.matweb.com/search/DataSheet.aspx?MatGUID=9f5318a1f93b403bbd5748abec70fac1&ckck=1`. Date accessed: August 2011.

[30] H. Gercek. Poisson's ratio values for rocks. *International Journal of Rock Mechanics and Mining Sciences*, 44(1):1–13, 2007.

[31] D.T. Blackstock. *Fundamentals of Physical Acoustics*. Wiley-interscience, 2000.

[32] S. Durvasula. Natural frequencies and modes of skew membranes. *The Journal of the Acoustical Society of America*, 44:1636, 1968.

[33] PCB Piezotronics. *Manual 130E Microphone Series*, 2003.

[34] G.L. Squires. *Practical Physics*. Cambridge Univ Pr, 2001.

[35] MatWeb L.L.C. ASTM A228. `http://www.matweb.com/search/DataSheet.aspx?MatGUID=4bcaab41d4eb43b3824d9de31c2c6849`. Date accessed: August 2011.

[36] F.P. Beer, E.R. Johnston, and J.T. DeWolf. *Mechanics of Materials*. McGraw Hill, 3rd edition, 2002.

[37] MatWeb L.L.C. AISI 1030 steel, as rolled. `http://www.matweb.com/search/DataSheet.aspx?MatGUID=7f9f243179b0490c812f5f540f93e7a3&ckck=1`. Date accessed: August 2011.

Vita

Thomas Frederick Pizarek spent most of his life in Austin, Texas, venturing to Indiana for his undergraduate studies, in which he pursued his interests in mathematics, science, and music. The Artium Baccalaureus degree in mathematics and physics was conferred upon him magna cum laude by Wabash College and he was inducted into Phi Beta Kappa in May of 2009. Following his graduation, he began graduate studies in the acoustics program within the Cockrell School of Engineering of the University of Texas at Austin in August, 2009.

Permanent address: tom.pizarek@utexas.edu

This thesis was typeset with LaTeX 2_ε by the author.